Far-field nanoscopy on a semiconductor quantum dot via a rapid-adiabatic-passage-based switch

Timo Kaldewey [1]*, Andreas V. Kuhlmann[1,3], Sascha R. Valentin[2], Arne Ludwig [2], Andreas D. Wieck [2] and Richard J. Warburton[1]

The diffraction limit prevents a conventional optical microscope from imaging at the nanoscale. However, nanoscale imaging of molecules is possible by exploiting an intensity-dependent molecular switch[1-3]. This switch is translated into a microscopy scheme, stimulated emission depletion microscopy[4-7]. Variants on this scheme exist[3,8-13], yet all exploit an incoherent response to the lasers. We present a scheme that relies on a coherent response to a laser. Quantum control of a two-level system proceeds via rapid adiabatic passage, an ideal molecular switch. We implement this scheme on an ensemble of quantum dots. Each quantum dot results in a bright spot in the image with extent down to 30 nm ($\lambda/31$). There is no significant loss of intensity with respect to confocal microscopy, resulting in a factor of 10 improvement in emitter position determination. The experiments establish rapid adiabatic passage as a versatile tool in the super-resolution toolbox.

Super-resolution techniques for imaging single quantum emitters rely on switching between two states: one is bright, the 'on' state, and the other is dark, the 'off' state[2,3]. These two states are typically different electronic states, but can also be different spin states[11]. Stimulated emission depletion microscopy (STED) is the prototypical scheme. In STED, the excited state, S_1, represents the 'on' state, and fluorescence results from radiative decay. The 'off' state is the ground state, S_0. The system can be transferred from the 'on' to the 'off' state by stimulated depletion with a red laser. The probability of the depletion process depends exponentially on the red laser power. In a highly simplified picture, the red laser acts as a switch: at low red intensities, the system remains in the 'on' state (strong fluorescence), and at high intensities the system transfers from the 'on' to the 'off' state (weak fluorescence). In STED microscopy, the red beam usually has a 'doughnut' intensity profile, and the spatial resolution is determined by the point at which the red power becomes sufficient to induce the transition from 'on' to 'off'[1,4,7,10]. Practical considerations and not diffraction per se limit the resolution. Many variants of the STED scheme have been developed. However, in all these schemes, the response to the lasers is incoherent: transitions between the two states are facilitated by transient occupation of intermediate states via incoherent processes.

We present an imaging scheme—rapid adiabatic passage (RAP) imaging—which relies instead on a coherent response to the laser. Transient population of other levels is not required. This strikes us as important. First, RAP imaging represents a new way of imaging coherent quantum optical systems on the nanoscale. Example systems include semiconductor quantum dots[14], colour centres[15] and single molecules[16], where in each case the optical transition

exhibits coherence at low temperature. Second, by manipulating quantum states coherently, the excitation of molecular vibrations (phonons in a solid-state context) is avoided. By way of contrast, in STED microscopy, hundreds of meV of energy are released into the molecule per cycle[4,6,17], which may lead to blinking and bleaching. Third, RAP is immune to spectral wanderings of the emitter, an advantageous feature whenever an emitter is located in a noisy environment.

The coherent response of a two-level system (TLS) to a pulse of resonant laser light is a Rabi oscillation. For instance, the system is driven from its ground state $|0\rangle$ to the excited state $|1\rangle$ ('pulse area' π) and then back to $|0\rangle$ ('pulse area' 2π) and so on (Fig. 1b). In terms of fluorescence, Rabi oscillations represent an off–on–off–on… behaviour as a function of intensity. If the TLS is illuminated with a high-intensity pulse with a Gaussian spatial profile, it leads to a series of rings in the optical response[18]. In other words, Rabi oscillations do not represent a simple on–off switch.

We propose that RAP is an excellent technique for imaging a TLS. In RAP, the laser frequency is swept through the TLS resonance during the laser pulse. RAP transfers the population from one state to the other, but without oscillations at large intensities (Fig. 1b). Applied to an ideal TLS initially in state $|0\rangle$, a weak RAP pulse leaves the system in state $|0\rangle$ whereas a strong RAP pulse transfers the system to state $|1\rangle$ (and vice versa for the system initially in state $|1\rangle$). The intensity dependence of RAP on a TLS represents a close to ideal on–off switch.

Our imaging scheme is depicted in Fig. 1. The TLS is initially in the ground state $|0\rangle$. A pulse with positive chirp and pulse area $> \pi$ is applied. This inverts the TLS provided it is located somewhere within the diffraction-limited spot, and it turns the system on. Subsequently, a pulse with negative chirp and pulse area $> \pi$ is applied. This pulse inverts the system a second time, leading to re-occupation of state $|0\rangle$, and it turns the system off. However, when the first pulse has a Gaussian spatial intensity distribution (termed here 'Gauss-pulse', Fig. 1c) and the second pulse a doughnut spatial intensity distribution (termed here 'doughnut-pulse', Fig. 1d), the second pulse is inactive at the centre of the doughnut. Under these conditions, the system is left in the 'on' state only when it is located close to the centre of the doughnut. The system then decays by spontaneous emission and the photon is detected. In this way, a fluorescence bright spot results at the centre of the doughnut. The spatial extent of the image is determined by the region in which the doughnut pulse area lies below π. In Stefan Hell's phrase, this represents a 'physics-based diffraction-unlimited' resolution[3].

RAP-based imaging has a number of key features. First, the scheme results in a single bright spot at the doughnut centre

[1]Department of Physics, University of Basel, Basel, Switzerland. [2]Lehrstuhl für Angewandte Festkörperphysik, Ruhr-Universität Bochum, Bochum, Germany. Present address: [3]IBM Research-Zurich, Rüschlikon, Switzerland. *e-mail: timo.kaldewey@unibas.ch
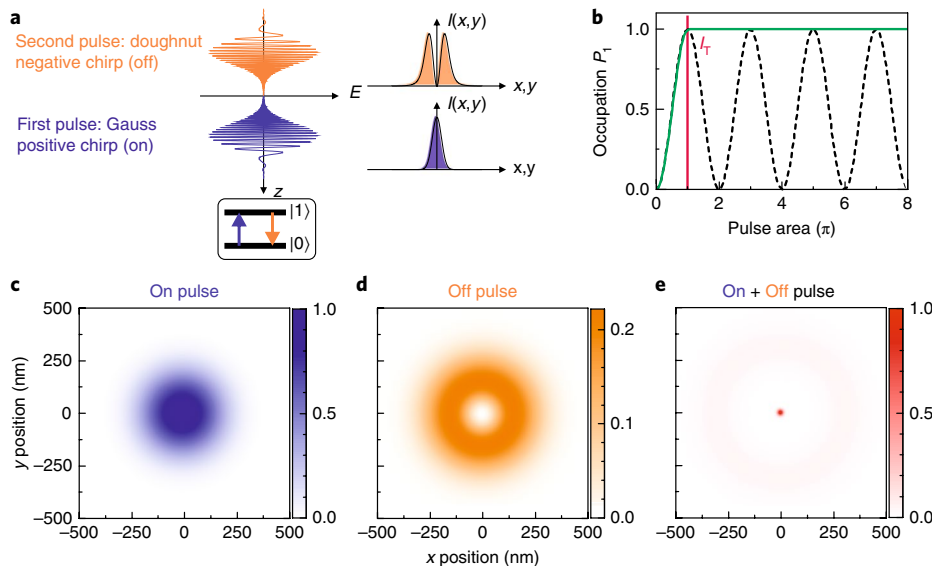
Fig. 1 | Concept of nanoscopic imaging of a quantum mechanical TLS. a, Temporal waveform and spatial intensity profile of the two optical pulses: excitation (positive chirp, Gaussian spatial profile, the 'Gauss-pulse') and de-excitation (negative chirp, doughnut spatial profile, the 'doughnut-pulse'). E, electric field, I intensity, (x, y) the lateral coordinates, z the longitudinal coordinate. **b**, Response of an ideal TLS to a single laser pulse. The system is initially in the ground state $|0\rangle$. Plotted is the occupation of the excited state $|1\rangle$, P_1, as a function of the square root of the intensity, parameterized in terms of the so-called 'pulse area' (time-integral of the Rabi frequency), defined such that the Rabi oscillation has a period of 2π. A resonant, unchirped pulse drives a Rabi oscillation (dashed black line). A chirped pulse (green solid line) transfers the system from state $|0\rangle$ to $|1\rangle$ for pulse areas above π by means of RAP. The intensity for a pulse area π is denoted I_T. **c–e**, Simulation of the imaging experiment (Gaussian optics for the two beams, the Landau–Zener formalism[32] for RAP): P_1 as a function of sample (x, y) position. **c**, Gauss-pulse only with $I_G^0 = 1I_T$. **d**, Doughnut-pulse only with $I_D^0 = 1I_T$. **e**, Gauss-pulse $I_G^0 = 3I_T$ followed by doughnut-pulse $I_D^0 = 205I_T$ resulting in a 14 times smaller spot size. The model for the simulation is described in Supplementary Section C. The following parameters were used here: wavelength 940 nm, refractive index solid immersion lens $n_{SIL} = 2.13$, beam diameter before the objective $\Delta X_{I,FWHM} = 2.0$ mm, focal length $f = 3.7$ mm, detection efficiency $\beta = 1$, chirp $\alpha_G = -\alpha_D = 3.24$ ps^{-2}.
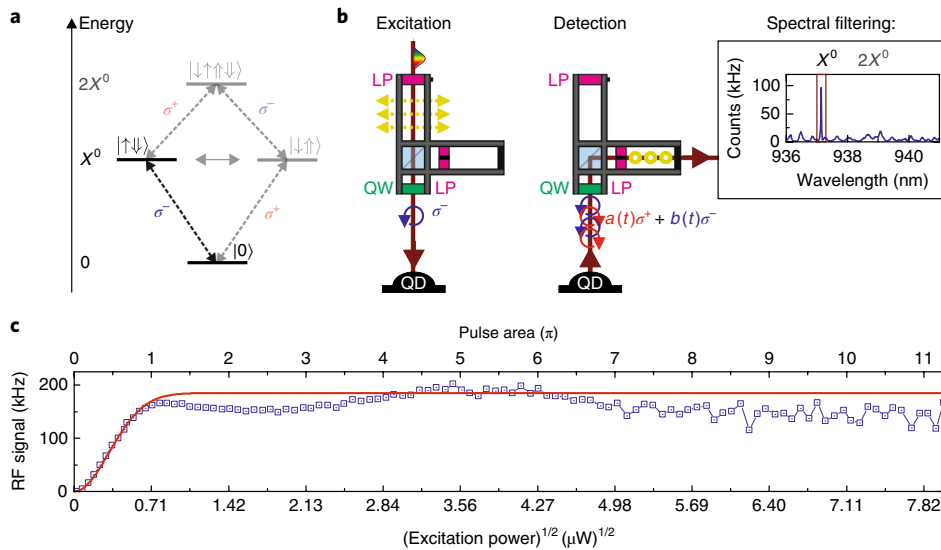
Fig. 2 | RAP on a single self-assembled QD. a, Energy level scheme of the QD: $|0\rangle$ represents the empty QD, $|1\rangle$ the spin-up exciton, $|1\rangle \equiv |\uparrow\Downarrow\rangle$. ($\uparrow$ ($\downarrow$) is a spin-up (spin-down) electron, $\Uparrow$ ($\Downarrow$) a spin-up (spin-down) hole.) Transition $|0\rangle \leftrightarrow |\uparrow\Downarrow\rangle$ is driven with left-handed circularly polarized light (σ^-). The two exciton states, $|\uparrow\Downarrow\rangle$ and $|\downarrow\Uparrow\rangle$, are coupled via the fine structure, which leads to a quantum beat $|\uparrow\Downarrow\rangle \leftrightarrow |\downarrow\Uparrow\rangle$ described by the time-dependent coefficients $a(t)$ and $b(t)$. On creating $|\uparrow\Downarrow\rangle$ with a σ^- polarized pulse, both σ^+ and σ^- polarized emission results. The biexciton state, $2X^0$, exists at higher energies but is not populated here. **b**, Polarization control in the dark-field microscope: the QD is excited with σ^- polarized light; σ^+ is detected. LP, linear polarizer; QW, quarter-wave plate. The detected signal is spectrally filtered. This increases the signal-to-background ratio. **c**, Resonance fluorescence versus pulse area (and square root of averaged excitation power P_{avg}) on a single, empty QD. Plotted is the detected emission from the $|X^0\rangle \rightarrow |0\rangle$ transition following circularly polarized excitation pulses (blue squares). The originally transform-limited pulses ($\tau_0 = 80$ fs) were positively chirped ($\phi_2 = 0.33$ ps^2) to a pulse duration of $\tau = 4$ ps (7 fs FWHM). Data are fitted to the Landau–Zener result (red line) with $A(1-\exp(-c^2\tau_0\sqrt{\tau_0^4 + \phi_2^2}/\phi_2 \times P_{avg}))$ and reveal $c\sqrt{\tau_0} = 4.4 \pm 0.2\,\mu\text{W}^{-1/2}$, in agreement with independently estimated values from Rabi oscillations ($4.4 \pm 0.4\,\mu\text{W}^{-1/2}$). Parameter c includes the dipole transition moment and, when multiplied with $\sqrt{\tau_0 P_{avg}}$, gives the pulse area.
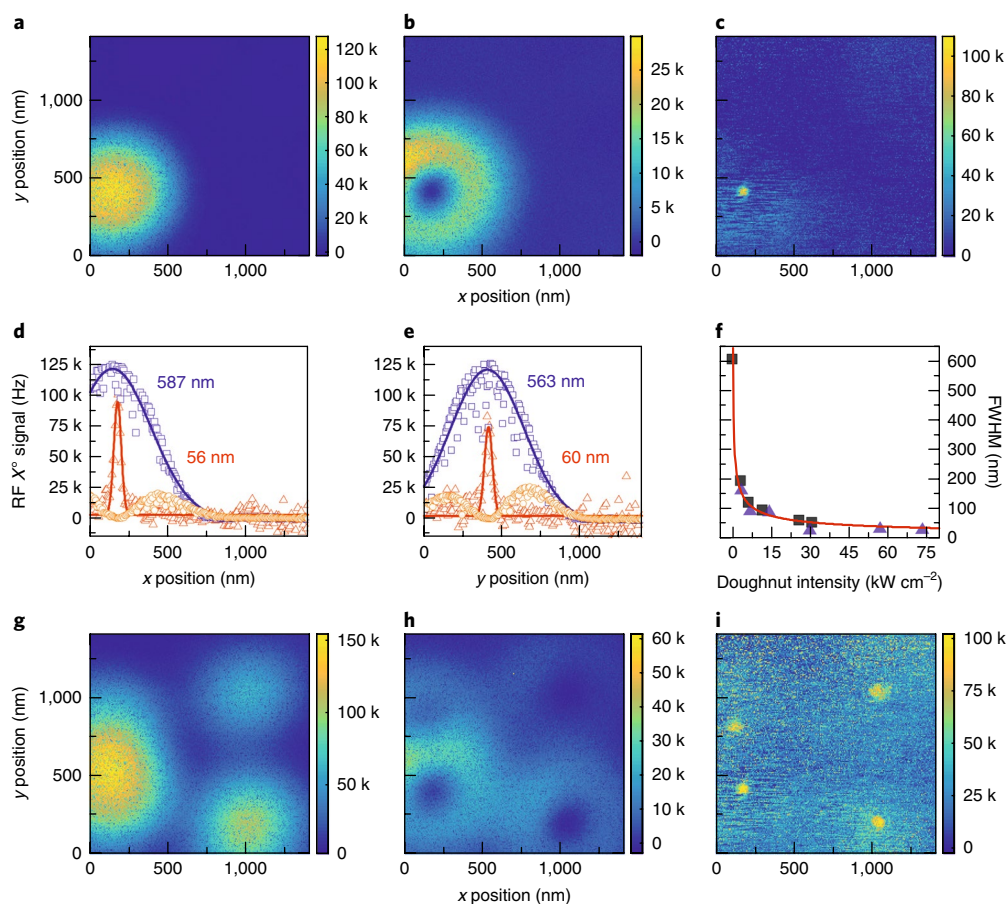
Fig. 3 | Imaging an ensemble of QDs with the RAP-based protocol. a–c, Resonance fluorescence as a function of sample position (x, y). Excitation intensities are stated in units of intensity $I_T = 0.28\,\text{kW cm}^{-2}$ (I_T corresponds to a power $P_T = 0.50\,\mu\text{W}$). **a**, Gauss-pulse only, intensity $I_G^0 = 1.2I_T$. **b**, Doughnut-pulse only, intensity $I_D^0 = 1.2I_T$. **c**, Gauss-pulse $I_G^0 = 2.8I_T$ followed by doughnut-pulse $I_D^0 = 205I_T = 57\,\text{kW cm}^{-2}$. Shown is the signal in a spectral window (wavelength bandwidth 0.05 nm) around the X^0 emission of one single QD. **d,e**, x and y line-cuts through the data in **a–c**, in blue (squares), orange (circles) and red (triangles), respectively. Solid lines are Gaussian fits to the blue and red data points. **f**, Extracted FWHM of the central image of one single QD as a function of the doughnut-pulse intensity I_D: $I_G = 1.2I_T$ (blue triangles) and $I_G = 2.8I_T$ (black squares). The smallest FWHM achieved here is 30 nm. **g–i**, Images from exactly the same region as in **a–c**, using exactly the same imaging parameters, but adding the signal from four integration windows (each with a width in wavelength of 0.05 nm): Gauss-pulse only (**g**); doughnut-pulse only (**h**); Gauss-pulse followed by doughnut-pulse (**i**). The images in **g–i** demonstrate the multiplexing capability of the imaging scheme: even when plotting signals from four different wavelengths simultaneously, individual QDs can be clearly resolved on account of the sub-diffraction resolution of each QD. The colour scale in **i** is slightly over-saturated to increase the contrast for less bright QDs.

(Fig. 1e and Supplementary Section C). In principle, there is no loss of intensity at the peak. This means that the accuracy of determining the emitter's position in a given time is enhanced by the ratio of confocal image size to RAP-based image size. At high powers, the scheme opens a new way of achieving a long-standing goal—imaging of an extended electron wavefunction with a far-field optical microscope[19]. Second, phonon creation (that is, heating) can be avoided in RAP by choosing positive chirp for the $|0\rangle \rightarrow |1\rangle$ process and negative chirp for the $|1\rangle \rightarrow |0\rangle$ process[20–22]. Third, while the chirped laser pulses are spectrally broadband, any spectral information of the emitter is retained. If the fluorescence from each emitter is narrowband, an inhomogeneous distribution of emitters (distribution in space or in time) can be addressed with the same laser pulses.

The main technical challenge in implementing RAP-based imaging is to distinguish the fluorescence from scattered laser light. This distinction can be made via the polarization (excitation and detection in orthogonal polarization states, Supplementary Section B2), the propagation direction (excitation and detection in different spatial modes), time-gating (switching the detectors on once the fast

laser pulses have exited) and the wavelength in the case of narrow-band emitters. Combinations of these options can be used simultaneously. We believe that the scheme can become a practical and versatile one.

We use quantum dots (QDs) to test RAP-based imaging. At low temperature with resonant optical driving, an InGaAs QD embedded in GaAs closely mimics a two-level atom (radiative lifetime of 800 ps, emission wavelength of 950 nm)[23–26]. State $|0\rangle$ is the crystal ground state (empty QD) and state $|1\rangle$ is the neutral exciton X^0 (electron–hole pair) (Fig. 2a). The chirped laser pulses are created from transform-limited laser pulses by introducing wavelength-dependent phase shifts (Supplementary Section B1). Unusually for QD experiments[21,27,28], we use the full bandwidth of a 130 fs laser pulse: this allows us to address almost all QDs in the sample with the same laser pulse. Figure 2c plots the resonance fluorescence as a function of pulse area on a single QD following excitation with a single laser pulse. The signal rises initially and is then roughly constant above a pulse area of π. The signal follows closely the Landau–Zener result for a TLS up to the maximum pulse area of 11π.

The RAP-based imaging proceeds by implementing the two-pulse scheme, creating an image by sample scanning. We collect the resonance fluorescence at the X^0 emission wavelength only (Fig. 3a–c). The Gauss-pulse alone gives an image, specifically a plot of resonance fluorescence versus position in the focal plane (Fig. 3a). Line-cuts through the image (Fig. 3d,e) show that the image is well described with a Gaussian function of position with mean full-width at half-maximum (FWHM) of 575 nm. This is the FWHM expected from diffraction in the collection optics of the microscope (for further details see Supplementary Information). Similarly, the response to the doughnut-pulse alone gives a doughnut-profile, again with an extent determined by diffraction (Fig. 3b). Applying both pulses sequentially breaks the diffraction limit: a bright spot emerges with FWHM of 56 nm in this particular experiment (Fig. 3c). The signal at the central bright spot is 80% of the signal with the Gauss-pulse alone. In terms of emitter position determination, analysis of the data in Fig. 3d,e shows that RAP-based imaging achieves a set localization resolution a factor of 10 times more quickly than confocal imaging.

The FWHM of the central image decreases with increasing doughnut-pulse intensity (Fig. 3f). This is the signature of imaging beyond the diffraction limit: it is the control of the on–off switching that determines the resolution, not the diffraction-limited focusing of the laser beams. The FWHM Δx follows the same functional form as for STED microscopy[6,29], $\Delta x(I_D) = \Delta x^o / \sqrt{1 + I_D / I_T}$ where Δx^o is the conventional diffraction limit, I_D the doughnut intensity and I_T the intensity at which the doughnut pulse area equals π (Supplementary Section C2). Here, we can anticipate $\Delta x(I_D)$ based only on characterization of the microscope performance (resonance fluorescence from a beam with Gaussian spatial profile at intensities well below saturation) and RAP characterization on the QD. The result describes the experimentally determined FWHM extremely well (Fig. 3f).

A key application of super-resolution microscopy is to garner an image with detail that is obscured in diffraction-limited microscopy. We demonstrate this by imaging a region of the sample containing a number of QDs separated laterally by distances smaller than or comparable to the diffraction limit of the microscope. An image with the Gauss-pulse alone, equivalently the doughnut-pulse alone, shows structure, but it is difficult to determine the number and location of individual emitters (Fig. 3g,h). With the RAP-based imaging, the number and location of emitters is clearly visible (Fig. 3i).

The RAP-based imaging in the present experiment is limited only by the technical difficulty of distinguishing the resonance fluorescence from the reflected laser light at the highest doughnut-pulse powers. This can be improved substantially in the future with time-gating. The RAP process on single QDs works well at 4 K: phonon emission is ruled out by choosing the chirp such that the lower branch in the RAP process is occupied (Supplementary Fig. 8), and phonon absorption is rendered weak by the small phonon population. We expect that RAP-based imaging will work effectively at higher temperatures, perhaps up to 50 K (ref. [22]): if RAP is carried out quickly enough, the inertia of the phonons prevents them from responding to the driven electron. RAP-based imaging can be applied immediately to other solid-state emitters with a coherent optical transition. It remains to be seen if this notion can be translated to imaging molecules in a bio-context.

Methods

Methods, including statements of data availability and any associated accession codes and references, are available at https://doi.org/10.1038/s41566-017-0079-y.

References

1. Hell, S. W. & Wichmann, J. Breaking the diffraction resolution limit by stimulated emission: stimulated-emission-depletion fluorescence microscopy. *Opt. Lett.* **19**, 780–782 (1994).
2. Betzig, E. et al. Imaging intracellular fluorescent proteins at nanometer resolution. *Science* **313**, 1642–1645 (2006).
3. Hell, S. W. Microscopy and its focal switch. *Nat. Methods* **6**, 24–32 (2009).
4. Klar, T. A., Jakobs, S., Dyba, M., Egner, A. & Hell, S. W. Fluorescence microscopy with diffraction resolution barrier broken by stimulated emission. *Proc. Natl Acad. Sci. USA* **97**, 8206–8210 (2000).
5. Dyba, M. & Hell, S. W. Focal spots of size λ/23 open up far-field florescence microscopy at 33 nm axial resolution. *Phys. Rev. Lett.* **88**, 163901 (2002).
6. Westphal, V. & Hell, S. W. Nanoscale resolution in the focal plane of an optical microscope. *Phys. Rev. Lett.* **94**, 143903 (2005).
7. Willig, K. I., Harke, B., Medda, R. & Hell, S. W. STED microscopy with continuous wave beams. *Nat. Methods* **4**, 915–918 (2007).
8. Bretschneider, S., Eggeling, C. & Hell, S. W. Breaking the diffraction barrier in fluorescence microscopy by optical shelving. *Phys. Rev. Lett.* **98**, 218103 (2007).
9. Hell, S. W. Far-field optical nanoscopy. *Science* **316**, 1153–1158 (2007).
10. Rittweger, E., Han, K. Y., Irvine, S. E., Eggeling, C. & Hell, S. W. STED microscopy reveals crystal colour centres with nanometric resolution. *Nat. Photon.* **3**, 144–147 (2009).
11. Maurer, P. C. et al. Far-field optical imaging and manipulation of individual spins with nanoscale resolution. *Nat. Phys.* **6**, 912–918 (2010).
12. Weisenburger, S. & Sandoghdar, V. Light microscopy: an ongoing contemporary revolution. *Contemp. Phys.* **56**, 123–143 (2015).
13. Balzarotti, F. et al. Nanometer resolution imaging and tracking of fluorescent molecules with minimal photon fluxes. *Science* **355**, 606–612 (2017).
14. Kuhlmann, A. V. et al. Charge noise and spin noise in a semiconductor quantum device. *Nat. Phys.* **9**, 570–575 (2013).
15. Sipahigil, A. et al. Indistinguishable photons from separated silicon-vacancy centers in diamond. *Phys. Rev. Lett.* **113**, 113602 (2014).
16. Wrigge, G., Gerhardt, I., Hwang, J., Zumofen, G. & Sandoghdar, V. Efficient coupling of photons to a single molecule and the observation of its resonance fluorescence. *Nat. Phys.* **4**, 60–66 (2008).
17. Hell, S. W. Toward fluorescence nanoscopy. *Nat. Biotechnol.* **21**, 1347–1355 (2003).
18. Gerhardt, I., Wrigge, G., Hwang, J., Zumofen, G. & Sandoghdar, V. Coherent nonlinear single-molecule microscopy. *Phys. Rev. A.* **82**, 063823 (2010).
19. Gräslund, A., Rigler, R. & Widengren, J. *Single Molecule Spectroscopy in Chemistry, Physics and Biology* (Series in Chemical Physics 96, Springer, 2010).
20. Lüker, S. et al. Influence of acoustic phonons on the optical control of quantum dots driven by adiabatic rapid passage. *Phys. Rev. B* **85**, 121302(R) (2012).
21. Wei, Y.-J. et al. Deterministic and robust generation of single photons from a single quantum dot with 99.5% indistinguishability using adiabatic rapid passage. *Nano Lett.* **14**, 6515–6519 (2014).
22. Kaldewey, T. et al. Demonstrating the decoupling regime of the electron-phonon interaction in a quantum dot using chirped optical excitation. *Phys. Rev. B* **95**, 241306(R) (2017).
23. Muller, A. et al. Resonance fluorescence from a coherently driven semiconductor quantum dot in a cavity. *Phys. Rev. Lett.* **99**, 187402 (2007).
24. Nguyen, H. S. et al. Ultra-coherent single photon source. *Appl. Phys. Lett.* **99**, 261904 (2011).
25. Matthiesen, C., Vamivakas, A. N. & Atatüre, M. Subnatural linewidth single photons from a quantum dot. *Phys. Rev. Lett.* **108**, 093602 (2012).
26. Kuhlmann, A. V. et al. A dark-field microscope for background-free detection of resonance fluorescence from single semiconductor quantum dots operating in a set-and-forget mode. *Rev. Sci. Instrum.* **84**, 073905 (2013).
27. Simon, C.-M. et al. Robust quantum dot exciton generation via adiabatic passage with frequency-swept optical pulses. *Phys. Rev. Lett.* **106**, 166801 (2011).
28. Wu, Y. et al. Population inversion in a single InGaAs quantum dot using the method of adiabatic rapid passage. *Phys. Rev. Lett.* **106**, 067401 (2011).
29. Harke, B. et al. Resolution scaling in STED microscopy. *Opt. Express* **16**, 4154–4162 (2008).
32. Shevchenko, S., Ashhab, S. & Nori, F. Landau–Zener–Stückelberg interferometry. *Phys. Rep.* **492**, 1–30 (2010).

Additional information

Supplementary information is available for this paper at https://doi.org/10.1038/s41566-017-0079-y.

Reprints and permissions information is available at www.nature.com/reprints.

Correspondence and requests for materials should be addressed to T.K.

Publisher's note: Springer Nature remains neutral with regard to jurisdictional claims in published maps and institutional affiliations.

Methods

The InGaAs QDs were embedded in a GaAs n–i–p diode (see Supplementary Section A)[30]. The heterostructure was grown by molecular beam epitaxy. Collection efficiency was increased by incorporating a semiconductor Bragg mirror below the QDs during heterostructure growth and by placing a solid immersion lens on the sample surface. The sample was a standard one for single-QD spectroscopy experiments. Resonance fluorescence was distinguished from back-scattered laser light by a polarization-based dark-field microscope[14,26] and by spectrally sensitive detection (for more details see Supplementary Section B). Specifically, we carried out excitation with circular polarization σ^- and detection with σ^+ (Fig. 2b). The spin ± 1 excitons were coupled together by some symmetry-breaking, leading to a quantum beat[31] between spin states $|+1\rangle$ and $|-1\rangle$ with period ~100 ps (Fig. 2a). This coupling resulted in σ^+ emission following σ^- excitation.

The laser was a mode-locked Ti:sapphire laser and produced close to transform-limited pulses with a duration of 130 fs (FWHM). The laser output was split into two beams, and two separate pulse-shapers introduced a controlled amount of chirp into the beams (for more details see Supplementary Section B1). One beam was delayed with respect to the other and then each beam was coupled into an optical fibre. The two optical fibres transported the beams to the two input ports of the microscope (for more details see Supplementary Section B2). Following collimation in the microscope, one of the beams passed through a 2π vortex phase plate. The two beams were then combined at a beamsplitter. The microscope objective, sample and nanopositioners were held at 4.2 K in a helium bath cryostat. The chirped pulses are well described by a Gaussian function of time, and the 'Gauss-pulse' is well described by a Gaussian function of the lateral coordinates in the focal plane of the microscope (for more details see Supplementary Information). In the focal plane, the beam with the phase-manipulated wavefront acquired a doughnut intensity profile. The doughnut maximum:minimum intensity ratio was larger than 1,000:1 (for more details see Supplementary Section B2). The microscope objective had a numerical aperture of 0.68 and operated close to the diffraction limit. Images were recorded by sample scanning. The acquisition time for the images shown in Fig. 3a–c,g–i, with 201×201 pixels was 5 h. The integration time per pixel was 25 ms, the total time per pixel (positioning time, dwell time and so on) was 155 ms, and two measurements per pixel were carried out.

Data availability. The data that support the plots within this paper and other findings of this study are available from the corresponding authors upon reasonable request.

References

30. Prechtel, J. H. et al. Decoupling a hole spin qubit from the nuclear spins. *Nat. Mater.* **15**, 981–986 (2016).
31. Tartakovskii, A. I. et al. Dynamics of coherent and incoherent spin polarizations in ensembles of quantum dots. *Phys. Rev. Lett.* **93**, 057401 (2004).